ADVANCED FUNCTIONAL MATERIALS
www.afm-journal.de

A Magnetoelastic Twist on Magnetic Noise: The Connection with Intrinsic Nonlinearities

Elizaveta Spetzler, Benjamin Spetzler,* and Jeffrey McCord*

Intrinsic magnetic noise limits the functionality of all magnetic field sensors and related devices using magnetic films as sensing elements. A novel origin of magnetic noise due to ferromagnetic material's magnetostriction is revealed by implementing a comprehensive multi-level signal-noise model and thoroughly validating it experimentally on magnetoelectric composite Δ*E*-effect sensors. From electrical measurements and operando magnetic domain visualization, magnetic contributions are shown to dominate the noise floor and limit the overall performance of multi-domain magnetoelastic sensors. The newly introduced noise contribution is correlated with the nonlinearity of the magnetostrictive properties. The effect on sensor output is particularly pronounced in magnetoelastic and magnetoelectric composite devices, but the results generally apply to all sensor devices incorporating magnetic materials. Therefore, the identified magnetic noise source makes a significant contribution to understanding the limitations of magnetic sensors and provides important guidelines for optimizing future magnetic sensors for low detectivity.

1. Introduction

Optimized soft magnetic materials and films are based on low magnetic anisotropy and near-zero magnetostriction.[1–3] On the other hand, it has been shown that nonzero magnetostriction can be beneficial for achieving low values of magnetic hysteresis in ferromagnetic films.[4,5] Ferromagnetic thin-film-based devices, especially magnetic field sensors, have numerous applications in the modern world, ranging from navigation systems to medical diagnostics and data storage applications.[6] These include magnetoresistive (XMR) sensors based on the anisotropic (AMR),[7–9] the giant (GMR),[10–14] and the tunnel magnetoresistive (TMR)[15–17] effects, mostly comprising magnetostrictive layer compositions for optimization of XMR effect strength or feasibility of fabrication. Other relevant sensor schemes are giant magnetoimpedance (GMI)[18–20] effect sensors and magnetoelectric (ME) composite sensors.[21–26] In this context, supporting flux concentrator structures[27–30] and magnetic shields[31,32] made of soft magnetic materials are also integrated into magnetic sensor structures based on non-ferromagnetic material, e.g., semiconductor-based Hall effect sensors.[33] For highly optimized XMR, GMI, and ME sensors, detectivities ≈1 pT/Hz$^{0.5}$ have been demonstrated.[19,34–36] However, the detectivity is mostly limited to higher magnetic field frequencies with limitations in the low-frequency or quasi-DC application regime. These limitations are partly overcome by modulation schemes to avoid the low-frequency flicker noise of the electronics.[37–40] Yet, correlated magnetic or magnetomechanical excitations lead to added performance limitations caused by additional intrinsic magnetic noise in the magnetic layers.[41–44]

Magnetic noise is a highly complex phenomenon, and understanding its origin has led to extensive research for various systems.[41,45,46] It has been shown that magnetic noise is strongly influenced by the magnetic configuration and operation parameters of the devices.[45,47–49] Depending on these, different shapes of, e.g., the voltage noise spectra have been observed,[43,50–52] generally following a $1/f^{\gamma}$ ($0 \leq \gamma \leq 2$) trend,[48,52,53] with f being the frequency. In the most commonly experimentally observed case with $\gamma \approx 1$,[41,49,54] magnetic noise exhibits magnetic $1/f$ or flicker noise characteristics. Numerous computational techniques have been used to simulate and explain the magnetic noise phenomena. Among these, stochastic atomistic simulations are considered to be the most physically accurate as they involve the fewest

E. Spetzler, J. McCord
Nanoscale Magnetic Materials – Magnetic Domains
Department of Materials Science
Kiel University
Kaiserstr. 2, 24143 Kiel, Germany
E-mail: elgo@tf.uni-kiel.de

B. Spetzler
Micro- and Nanoelectronic Systems
Institute of Micro and Nanotechnologies MacroNano
Technische Universität Ilmenau
Ehrenbergstr. 29, 98693 Ilmenau, Germany
E-mail: benjamin.spetzler@tu-ilmenau.de

B. Spetzler
Institute of Micro and Nanotechnologies MacroNano
Ehrenbergstr. 29, 98693 Ilmenau, Germany

J. McCord
Kiel Nano
Surface and Interface Science (KiNSIS)
Kiel University
Christian-Albrechts-Platz 4, 24118 Kiel, Germany

The ORCID identification number(s) for the author(s) of this article can be found under https://doi.org/10.1002/adfm.202309867

DOI: 10.1002/adfm.202309867

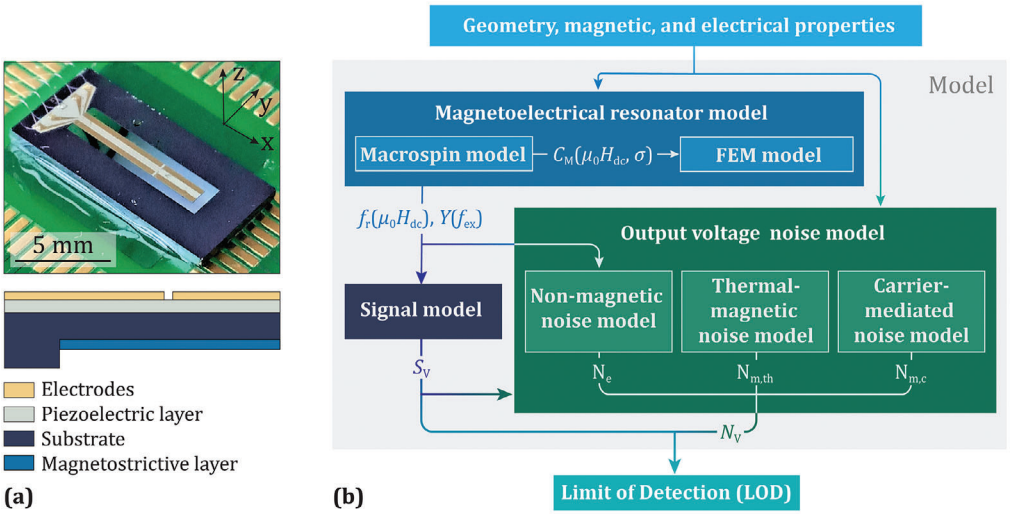

Figure 1. a) Photograph and cross-sectional schematic of the example ΔE-effect sensor. b) Flowchart of the combined sensor system model. The three main parts of the model are shown: the magnetoelectrical resonator model, the signal model, and the noise model. The corresponding sub-models are indicated. The input properties are used for all parts of the model. The main output of the model is the resulting limit of detection (LOD) of the sensor. Important intermediate results of the simulations are indicated, such as the sensitivity $\boldsymbol{S_V}$ and output voltage noise density N_V. (See Experimental Section for details).

approximations.[55,56] This method requires a spatial and temporal discretization on atomistic scales, accompanied by a big computational effort.[57,58] Therefore, linear macrospin models based on the fluctuation-dissipation theorem (FDT)[41,59–61] are now widely used to approximate thermal magnetic noise. The primary assumption of such models is that magnetic noise is caused solely by thermally activated fluctuations of magnetization.

Here, we provide evidence for the existence of an additional magnetic noise mechanism related to the inherent magnetostriction of the applied ferromagnetic materials. The additional noise mechanism becomes particularly important when dealing with magnetostrictive devices:[62,63] such as actuators,[64] antennas,[26,65,66] data storage elements,[67,68] pressure sensors,[69–71] and magnetic field sensors.[53,72–74] Magnetic noise theory is applied to describe ΔE-effect sensors as an example of modulated magnetoelastic magnetic field sensors.[75] The extended theory is implemented in a comprehensive multi-level sensor system model and thoroughly validated with measurements. In particular, we demonstrate the critical influence of the nonlinearity of magnetoelasticity on the sensor output noise for magnetic thin-film-based devices.

2. Results and Discussion

2.1. Sensor Concept

The magnetic field sensor used here is a magnetoelectric composite ΔE-effect sensor with a $(Fe_{90}Co_{10})_{78}Si_{12}B_{10}$ amorphous magnetostrictive ferromagnetic sensing layer. A photograph and the schematics of the sensor are shown in **Figure 1a**. The operating principle of the sensor is based on the dependence of the stiffness tensor C_M of the ferromagnetic layer on its magnetic configuration.[76] During sensor operation, the cantilever is electrically excited at or near its mechanical resonance frequency f_r by applying the time t dependent voltage $u_{ex}(t) = |u_{ex}| \sin(2\pi f_{ex} t)$ with frequency $f_{ex} \approx f_r$ and base-to-peak amplitude $|u_{ex}|$. The excitation voltage u_{ex} and the current $i_s(t) = Y u_{ex}(t)$ through the sensor element are connected via the electrical admittance Y of the device, which is defined by the electrical, mechanical, and magnetic properties of the sensor element. An external and varying magnetic sensing field $\mu_0 H_{ac}$ changes the orientation of the magnetization M in the magnetostrictive sensing layer, and therefore changes the stiffness of the cantilever and its admittance Y. The change in admittance Y modulates the current $i_s(t)$, which is then amplified with a charge amplifier allowing for magnetic field detectability (limit of detection, LOD) down to the 100 pT/Hz$^{0.5}$ regime (a description of the sensor and its operation is provided in the Experimental Section).[75]

2.2. Sensor Model

An overview of the full model to describe the signal and noise performance of magnetoelastic ΔE-effect sensors is shown in Figure 1b. The model covers all levels of the sensor system, from the physical properties of the resonator to the electric circuit representation of signal and noise. Only this approach makes it possible to relate the design and operating parameters to the device's performance in terms of signal, noise, and LOD of the sensor system.

In the model, we simulate the magnetoelastic resonator by combining magnetic macrospin and finite-element-method (FEM) models. With the macrospin model, we calculate the stiffness tensor C_M of the magnetostrictive layer as a function of the applied magnetic bias field $\mu_0 H_{dc}$ and stress σ. The obtained values of C_M are then used for the FEM simulations. With these joint models, we are able to describe the coupled magnetic, magnetoelastic, and electromechanical properties of the cantilever, such as $Y(f_{ex})$ and $f_r(\mu_0 H_{dc})$. In a further step, the resonator model is coupled to an analytical signal model and an output voltage noise

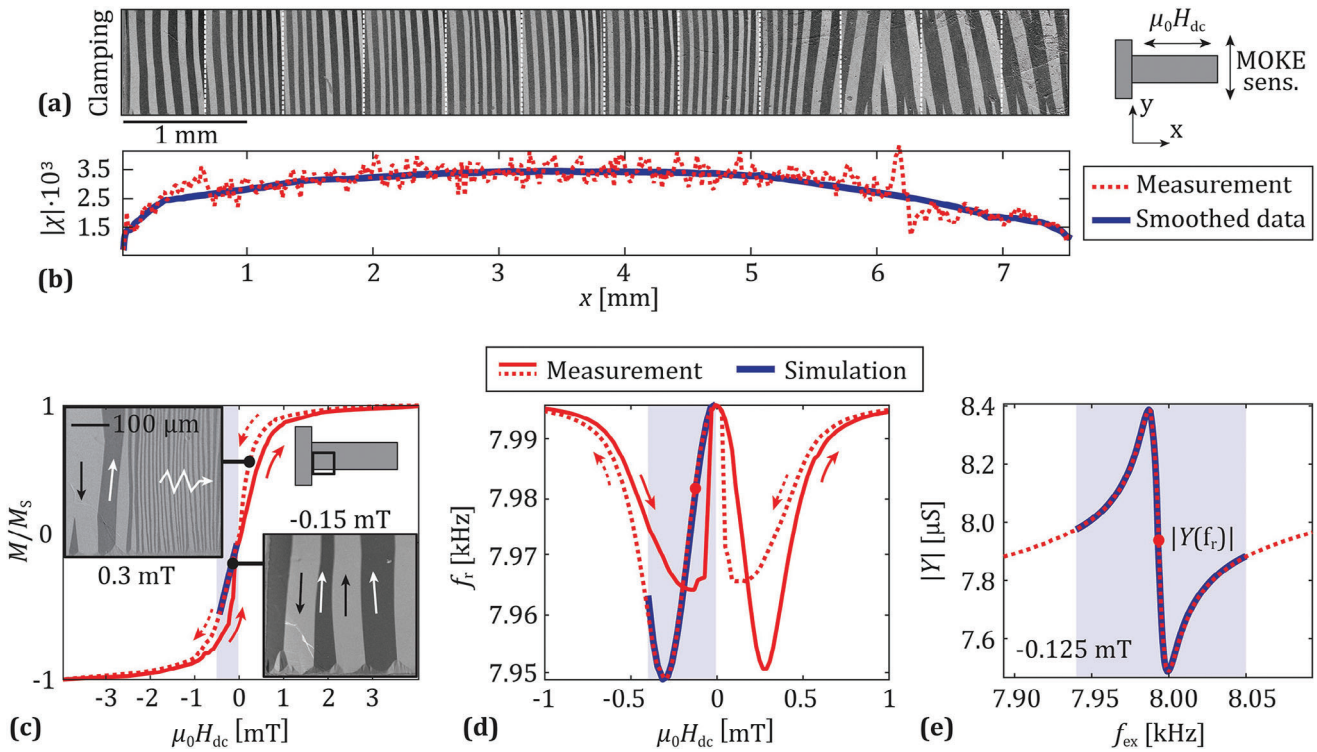

Figure 2. Magnetic and electrical properties of the sample. a) MOKE micrograph of the sample after demagnetizing along the x-axis. The MOKE sensitivity axis (MOKE sens.) was aligned perpendicular to the applied field axis. The picture is composed of several separate images (as indicated). b) The distribution of the differential magnetic susceptibility at $\mu_0 H_{dc} = -0.125$ mT across the sample extracted from local magnetization curve measurements with a magnetic field $\mu_0 H_{dc}$ applied along the x-axis. c) Magneto-optically recorded magnetization loop and corresponding two magnetic domain configurations at $\mu_0 H_{dc} = 0.3$mT and $\mu_0 H_{dc} = -0.15$mT, respectively. The magnetization curve and the domain images were recorded at the clamping region of the cantilever, as shown. The external magnetic field $\mu_0 H_{dc}$ is applied along the x-axis. The MOKE sensitivity axis was aligned parallel to the applied field axis for recording the magnetization loops. d) Measurement and FEM simulation of the change in the resonance frequency f_r as a function of $\mu_0 H_{dc}$. e) Measurement and FEM simulation of the sensor admittance magnitude $|Y|$ as a function of the excitation frequency f_{ex} at $\mu_0 H_{dc} = -0.125$ mT.

model by combining equivalent-electrical-circuit and macrospin-based models. The calculated sensitivity S_v and noise(s) N are then eventually combined to obtain the LOD of the sensor system.

2.3. Sensor Performance

2.3.1. Magnetoelectrical Resonator: Experiment and Simulations

The local magnetic properties required for the resonator model were extracted from magnetooptical Kerr effect (MOKE) microscopy measurements.[77] As visible from the magnetic domain structure in **Figure** 2a, the effective magnetic anisotropy of the sample is mainly aligned along the short axis of the cantilever. However, the variation in domain width and misorientation of the domain walls at the cantilever tips indicate a local variation of magnitude and orientation of effective uniaxial magnetic anisotropy. To quantify the resulting distribution of effective susceptibility, we measured local magnetization curves along the cantilever length. From this, we determined the local differential magnetic susceptibility χ at bias fields from $\mu_0 H_{dc} = -0.075$ mT to $\mu_0 H_{dc} = -0.175$ mT with a saturation magnetization of $\mu_0 M_S = 1.48$ T.[76] The variation of the magnitude of χ along the length of the cantilever is shown in Figure 2b. In addition to the slightly varying magnetic anisotropy, the susceptibility drops at the edges due to the spatially increasing demagnetizing field.[78]

An example magnetization curve of the sample recorded at the clamping region is plotted in Figure 2c. The magnetization curve shows notable hysteresis openings in the positive and negative magnetic field range characteristic for the intermediate occurrence of a blocked narrow magnetic domain state ($\mu_0 H_{dc} = 0.3$ mT)[79–82] forming after saturation. During the reversal, the metastable low susceptibility state breaks down via a swift reorganization of the domain structure.[83] The system transitions to a domain state close to its ground state ($\mu_0 H_{dc} = -0.15$ mT). As a consequence, these domain processes lead to a notably hysteretic and asymmetric resonance frequency $f_r(\mu_0 H_{dc})$ curve (Figure 2d). At $\mu_0 H_{dc} \approx 0.02$ mT a discontinuity is visible, correlating with the breakdown of the blocked state. Note that the discontinuous domain-state transition is irreversible and therefore the steep alteration of $f_r(\mu_0 H_{dc})$ is not suitable for sensor operation. For measurements and simulations, we use the magnetic field values $\mu_0 H_{dc} < 0$ mT (after saturation in the positive magnetic field).

Using a resonator model, we calculate the admittance characteristics and the resonance frequency f_r of the cantilever as a function of $\mu_0 H_{dc}$. Using the obtained magnetic property and

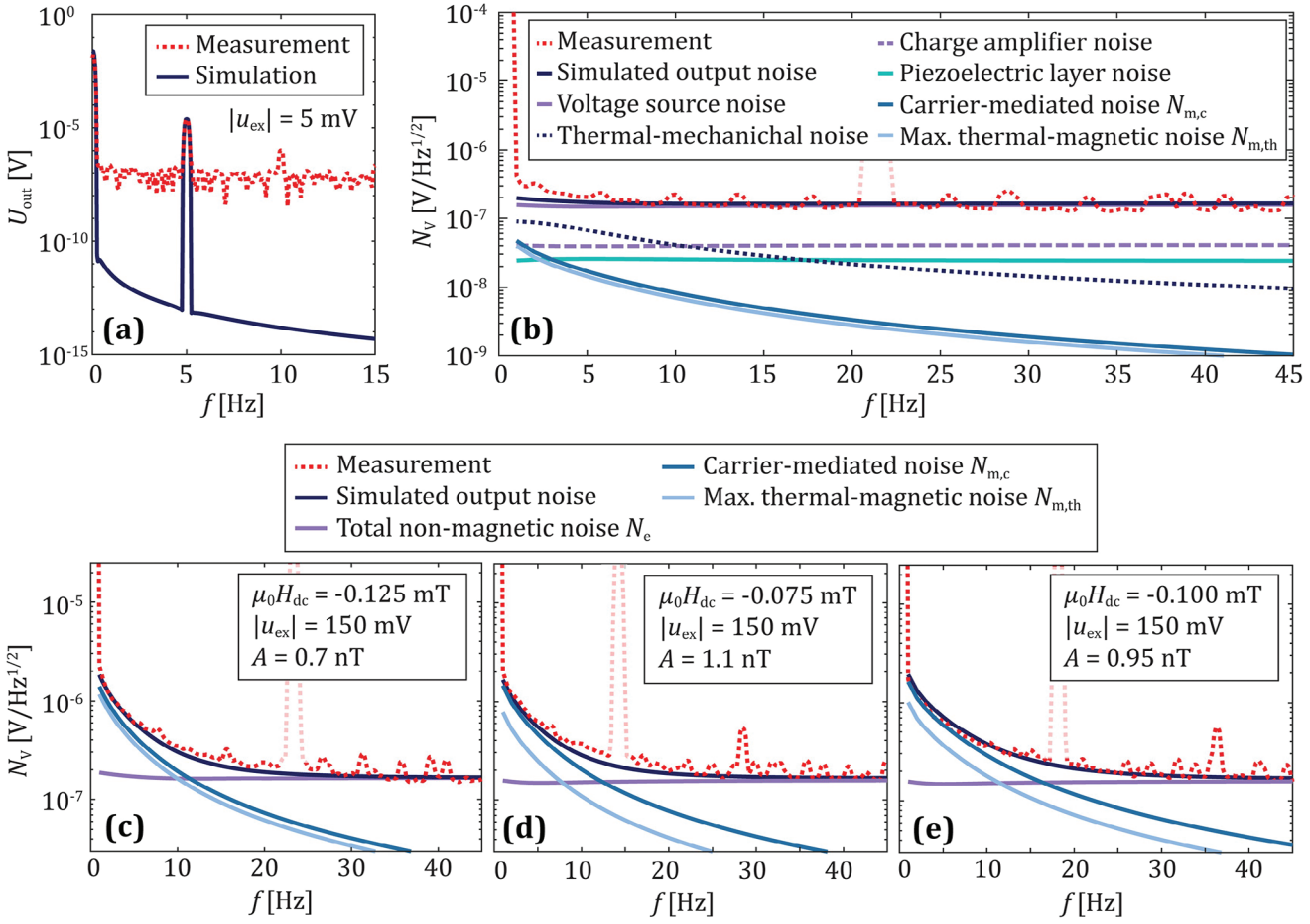

Figure 3. Comparison of measured and simulated signal and noise. a) Measured and simulated demodulated output voltage for a test magnetic field signal $\mu_0 H_{ac}$ = 500 nT with f_{ac} = 5 Hz applied externally at $\mu_0 H_{dc}$ = − 0.125 mT. b–e) Measured and simulated demodulated voltage noise density for $\mu_0 H_{dc}$ = − 0.125 mT (b,c), $\mu_0 H_{dc}$ = − 0.075 mT (d), and $\mu_0 H_{dc}$ = − 0.1 mT (e) bias fields. The output-referred noise density from the non-magnetic sources is calculated using the equivalent electrical circuit model presented earlier.[42,84] Magnetic noise is calculated with Equations 11 and 12 using the sensitivity calculated with Equation 7 (see Experimental Section).

the mechanical data as an input, the simulations match the measurements of $f_r(\mu_0 H_{dc})$ around the operating point $\mu_0 H_{dc} \cong -$ 0.125 mT (Figure 2d) as well as the sensor admittance magnitude $|Y|$ around f_r in the whole frequency range (Figure 2e). From these data, we can calculate the electrical and magnetic sensitivity of the cantilever for the signal model.

2.3.2. Signal, Noise, and Limit of Detection

Signal and noise measurements of the sensor were performed for varying excitation voltage amplitudes $|u_{ex}|$ and magnetic bias fields $\mu_0 H_{dc}$. Signal and noise measurements and simulations performed at a small excitation voltage $|u_{ex}| = 5$ mV and $\mu_0 H_{dc} = -$ 0.125 mT are shown in **Figure** 3a,b. Figure 3a shows that the signal model based on the data obtained from the resonator model reproduces the carrier and the signal peak very accurately. A close agreement between measurements and simulations is also observed for the noise data (Figure 3b). The simulated amplitude noise densities of the considered magnetic and non-magnetic noise sources demonstrate their individual contributions to the total noise floor (Figure 3b). At small $|u_{ex}|$ the electric noise sources dominate, resulting in an almost white noise spectrum. The additional peak that is faintly visible in the measurement curves is caused by internal distortions in the excitation source and does not affect the overall noise floor.

The results of additional measurements and simulations for two other magnetic bias fields as well as for a larger excitation voltage amplitude of $|u_{ex}| = 150$ mV but with the same magnetic bias field are shown in Figure 3c–e. Far from the carrier, the total noise spectrum N_V is in all cases still dominated by the white noise of the excitation voltage source. However, at smaller frequencies close to the carrier, the noise floor varies with $|u_{ex}|$ and $\mu_0 H_{dc}$. In all three examples, low-frequency noise is dominated by the carrier-mediated magnetic noise $N_{m,c}$.

For the shown simulations, we assumed the maximum possible value of the thermal magnetic noise $N_{m,\,th}$ ($\chi = \chi''$ in Equation 10), which means that all energy introduced into the system is immediately dissipated as heat. However, even considering such a boundary case, the large noise levels measured around the carrier can only be explained together with the additional carrier-mediated magnetic noise contribution (Figure 3d,e).

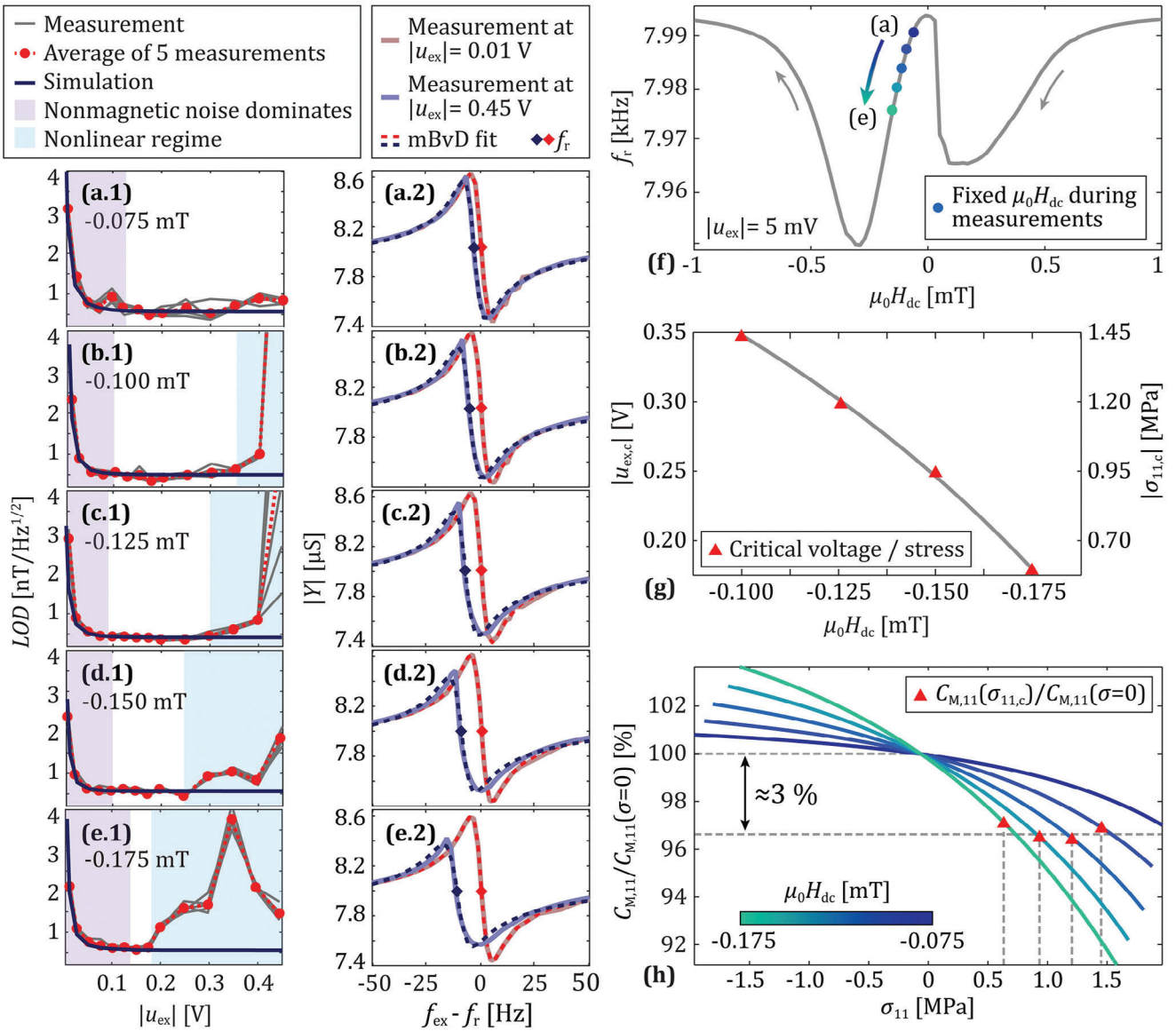

Figure 4. Contributions of different noise sources and nonlinearities to the LOD of the sensor. a.1–e.1) measured and simulated LOD over the excitation voltage amplitude for various $\mu_0 H_{dc}$ and f_{ac} = 5 Hz. a.2–e.2) Measured sensor admittance over the excitation frequency f_{ex} for two excitation voltage amplitudes $|u_{ex}| = 0.01$ V and $|u_{ex}| = 0.45$ V. The data are fitted with the mBvD model.[40,85] f) Dependency of the resonance frequency f_r of the cantilever on the magnetic bias field $\mu_0 H_{dc}$. The values of $\mu_0 H_{dc}$ used in the measurements (a–e) are indicated. g) Dependency of the critical excitation voltage amplitude $|u_{ex,c}|$ and its corresponding critical stress amplitudes $|\sigma_{11,c}|$ at which the third (nonlinear) operation regime starts as a function of the magnetic bias field $\mu_0 H_{dc}$. The parabolic fit provides a guide to the eye. h) Estimated dependency of the normalized $C_{M,11}$ component of the stiffness tensor C_M on the stress σ_{11} along the X-axis for different values of $\mu_0 H_{dc}$.

Furthermore, to achieve a good match between the simulations and the measurements, the pre-factor A in the carrier-mediated noise (Equation 12) was considered to depend on the applied bias field $\mu_0 H_{dc}$. As shown in Figure 3c–e the values of A decrease with decreasing $\mu_0 H_{dc}$. For even smaller magnetic field amplitudes, we observed an increase in A (not shown), which correlates with the changing areas of the domain wall activity (Figure S2, Supporting Information).

In the following, the dependence of the signal and the noise on voltage amplitude is analyzed in more detail. For this, the LOD at f_{ac} = 5 Hz was measured and simulated for five different magnetic bias fields $\mu_0 H_{dc}$ from −0.075 to −0.175 mT (**Figure** 4a.1–e.1). At each bias field value, the excitation voltage amplitude $|u_{ex}|$ was ramped up from 5 mV to 0.45 V. At each field, the measurement was repeated 5 times (grey curves) and then averaged (red curves). A general trend is visible in the LOD for all five magnetic bias fields, and three different regimes can be identified as a function of $|u_{ex}|$. At low excitation voltages, the nonmagnetic noise sources dominate the noise floor. In this regime, they are independent of the excitation voltage amplitude $|u_{ex}|$, while the sensitivity S_V increases linearly with $|u_{ex}|$ (Equations 5 and 7). This results in a $LOD \propto 1/|u_{ex}|$ dependence (purple regions

in Figure 4a.1–e.1). For moderate $|u_{ex}|$ (white regions), magnetic noise $N_{m,th} + N_{m,c}$ dominates. Since the magnetic noise and S_V scale linearly with $|u_{ex}|$ (Equations 11 and 12) the LOD remains constant in this regime. In the third regime of high excitation voltage amplitudes (blue regions), beyond a critical excitation amplitude $|u_{ex,c}|$, the noise floor starts to increase, leading to a degradation of the LOD together with a significant scatter in LOD. Most notably, as the magnetic bias field is reduced, the onset of the third regime occurs at a progressively smaller $|u_{ex}|$, which correlates with a change we observe in the admittance characteristics. Figure 4a.2–e.2 shows the admittance curves of the sensor at the small ($|u_{ex}| = 0.01$ V) and high ($|u_{ex}| = 0.45$ V) excitation voltage amplitudes at the five different magnetic bias fields. With increasing $|u_{ex}|$, the admittance curves shift to lower frequencies and become more asymmetric. This is a characteristic behavior for nonlinear resonators. This becomes particularly evident when the measured data are compared with the linear modified Butterworth van-Dyke (mBvD) model.[40,85] The deviations from the model increase with decreasing magnetic bias field $\mu_0 H_{dc}$ as the resonator becomes more nonlinear as the operation point moves towards the minimum of the resonance frequency curve (Figure 4f).

Overall, it can be noted that the simulations match the measured LOD in the first and second regimes of $|u_{ex}|$, where the resonator behaves linearly. In the third regime, the simulated LOD remains constant and does not reflect the experimentally observed degradation. This discrepancy is mainly due to a deviation of the simulated noise (see Supporting Information) and not due to a significant deviation of the signal model.

To gain insights into the microscopic origin of this noise source, we performed operando time-resolved dynamic MOKE microscopy measurements at the clamping region of the resonator, where the stress and its gradient are the largest. While modulation of the magnetization and motion of the domain walls are visible, no signs of domain rearrangements or domain wall hopping were observed during device operation. The movement of domain walls scales nearly linear with $|u_{ex}|$. No onset or nonlinear magnetic domain wall activity with increasing $|u_{ex}|$ is found from the active device imaging that could explain the measured surge in the noise level (see Supporting Information).

2.3.3. Nonlinearity of the ΔE Effect

The nonlinearity results from magnetostriction, which is confirmed by additional admittance measurements in magnetic saturation (see Supporting Information). The measurements also show that other possible nonlinear effects are negligible. The observed nonlinearity in our sensor is consistent with previous studies on magnetoelastic nonlinearities in magnetoelectric resonators.[85–87]

During excitation, time-dependent stress-induced magnetic anisotropy alters the magnetic state of the magnetostrictive layer, which, as a result, also changes the stiffness of the cantilever. In our model, however, we assumed that the stiffness of the resonator depends only on the magnetic bias field and that the cantilever behaves like a harmonic oscillator. As shown by the nearly perfect agreement of simulations and measurements, this is a valid assumption for small and moderate excitation voltages. However, at higher excitation voltages, the nonlinear contribution of magnetostriction to the stress-strain curve must be considered.

As a measure of the nonlinearity, we calculate the dominant component $C_{M,11}(\sigma_{11})$ of the stiffness tensor as a function of the stress component σ_{11} along the cantilever for the five magnetic bias fields discussed in Figure 4a–g. The results are normalized to $C_{M,11}(\sigma_{11} = 0)$ and shown in Figure 4h within the stress range that occurs during the oscillation of the resonator near the middle of the cantilever where the differential magnetic susceptibility χ is at maximum and σ_{11} reaches its second maximum. The critical stress amplitudes $|\sigma_{11,c}|$ at which the nonlinear regime starts (from Figure 4a.1–e.1) are indicated. A significant change in the normalized stiffness tensor component is evident for all magnetic bias fields, with a more pronounced change at smaller fields. The model proves an increasing nonlinearity as the magnetic bias field moves towards the minimum of the resonance frequency curve in Figure 4f. This is consistent with the admittance measurements.

The onset of nonlinearity is at approximately the same level of $C_{M,11}/C_{M,11}(\sigma_{11} = 0)$ for all magnetic bias fields. It occurs at about $C_{M,11}/C_{M,11}(\sigma_{11} = 0) \approx 3\%$ change in the normalized stiffness tensor component. The change of 3 % is reached at different stress values σ_{11}, and therefore, also different stress gradients $\nabla\sigma_{11}$ in the magnetostrictive layer. The maximum change of magnetization induced by the stress during the oscillation also depends on the magnetic bias field and follows a clear trend (see Supporting Information). The sharp onset of noise with $|u_{ex}|$ cannot be traced back to a threshold in the stress-induced magnetoelastic anisotropy, the amplitude of the driving forces for the motion of domain walls, or the induced change in magnetization.

3. Conclusion

A complete theory is used to describe magnetic noise in magnetic film-based sensor systems. It also includes magnetomechanical terms, and in particular, the magnetoelastic material properties are taken into account. A ΔE-effect magnetic field sensor is analyzed as a representative system. The comparison of multi-level simulations and measurements reveals that thermal-magnetic noise is insufficient to describe the intrinsic magnetic noise of the sensor. An additional magnetic noise source mediated by the electromechanical excitation is needed to accurately describe the performance of the multi-domain sample. The phenomenological expression for this carrier-mediated magnetic noise is derived and validated by the excellent match of measured signal, noise, and limit of detection with simulations. By taking into account non-magnetic and magnetic noise sources, the detailed analysis reveals previously unrecognized sensor-intrinsic magnetic noise sources that are fundamentally associated with the properties of magnetoelasticity.

The carrier-mediated noise model is consistent with noise measurements on similar sensors with a magnetostrictive FeCoSiB/Cr multilayer stack as the magnetoelastic sensor component.[42] There, the overall noise level of the multilayer device is notably lower than in our single-layer sensor, which is consistent with the different magnetic domain behavior in the laminated stack. Closure domains present in the single-layer sample increase the number of domain walls n_{dw} compared to

the magnetic multi-layer sample, and therefore, increase the carrier-mediated magnetic noise $N_{m,c}$ (Equation 12). Moreover, domain wall parameters are significantly different in the laminated multilayers.[88–90] Lower domain wall energy and the related change in domain wall width result in reduced domain wall pinning,[91] leading to magnetic noise reduction. This behavior is consistent with the analysis presented here. In addition, the domain wall energy depends on the magnetic bias field,[80] which is reflected in the observed change in the prefactor A in the carrier-mediated noise simulations. Carrier-mediated magnetic noise is not responsible for the sudden increase in intrinsic sensor noise at larger excitation voltage amplitudes. Sudden and discrete rearrangements of the magnetic domain structures as a mechanism can be ruled out for our measurements as operando time-resolved MOKE microscopy shows no dramatic increase in magnetic domain rearrangements during sensor operation.[53] No Barkhausen noise-attributed jumps in the sensor output signal were observed. The results clearly indicate the presence of a so-far unidentified magnetic noise source strongly connected with magnetoelastic nonlinearity effects.

Our study provides robust theoretical and experimental evidence for the origin of magnetic noise. Reducing carrier-mediated noise through a strategic magnetic layer and domain engineering and implementing techniques such as exchange-bias schemes are expected to play a crucial role in improving the performance of modulated film-based magnetic field sensors. However, it is important to note that the nonlinear characteristics of magnetostriction and the discovered influence on device properties impose significant limitations on functional devices that rely on ferromagnetic thin films as their sensitive components.

To conclude, we present a magnetic noise theory for magnetoelastic materials and reveal previously unrecognized noise sources caused by the magnetoelasticity of magnetic layers. Significant insights into the origin of the noise sources are gained with solid evidence for a direct link to the intrinsic magnetoelastic nonlinearity. As such, this work makes a significant contribution to the understanding of the inherent limitations of magnetoelastic systems and provides important guidance for future functional device optimizations.

4. Experimental Section

Sensor Preparation and Operation: A photograph and an illustration of the structure of the ΔE-effect sensor used in this paper are shown in Figure 1a. The cantilever was 7.5 mm long, 1 mm wide, and comprised a 50-µm-thick poly-Si substrate, a 2-µm-thick AlN piezoelectric layer sandwiched between a bottom and four top 150-nm-thick Ta/Pt electrodes, and a 500-nm-thick $(Fe_{90}Co_{10})_{78}Si_{12}B_{10}$ amorphous magnetostrictive ferromagnetic layer (saturation magnetostriction $\lambda_S \approx 35$ ppm).[92] During the deposition of the magnetic layer, a magnetic bias field of $\mu_0 H \approx 10$ mT was applied to induce a uniaxial magnetic anisotropy along the short axis of the cantilever. All measurements and simulations were carried out in the second bending mode using the two long electrodes close to the clamping. These electrodes had a width of 0.3 mm and a length of 5 mm. Details about the MEMS fabrication process and materials can be found in the previous work.[40]

FEM Simulation of the Magnetoelectrical Resonator: A 3D finite element method (FEM) model is set up in COMSOL Multiphysics v.6.0. to describe the resonator's electromechanical and magnetoelastic response. The model coupled the linear mechanical equations of motion[93] to the electrostatic equations[94] via the piezoelectric constitutive relations.[95] The sinusoidal excitation voltage $u_{ex}(t) = |u_{ex}| \sin(2\pi f_{ex} t)$ was applied as a Dirichlet boundary condition for the potential at the top electrode, the rear side electrode was defined as electrical ground, and fixed boundary conditions were used for the displacement field at the cantilever clamping. The system of equations was solved in the frequency domain for the mechanical displacement field and the electrostatic potential. The change ΔC_M of the stiffness tensor of the ferromagnetic layer was included in the model as a function of the magnetic bias field $\mu_0 H_{dc}$ and space to consider magnetic inhomogeneities.[96] For the calculation of the local stiffness tensor, the x-dimension was discretized into 100 elements of different widths with a refined discretization at the clamping and tip of the cantilever. Consequently, the components $C_{M,ij}(M(\mu_0 H_{dc},x))$ of the effective stiffness tensor were considered as functions of the applied magnetic field, intrinsic magnetic anisotropy, stress-induced anisotropy, and location along the cantilever. The same discretization was used for calculating the spatially averaged thermal-magnetic noise density. The components of ΔC_M were derived by linearizing the stress–strain relationship around the equilibrium magnetization M.[96] From the simulations, we obtain the sensor admittance $Y(f_{ex},\mu_0 H_{dc})$ as a function of the excitation frequency f_{ex} and the magnetic bias field $\mu_0 H_{dc}$, as well as the resonance frequency $f_r(\mu_0 H_{dc})$. Both functions are essential inputs for the signal model and the noise model. The mechanical and electrical material properties used in the FEM model are provided in Table S1 and Equations S8 and S9 (Supporting Information). For the stress–strain simulations in Figure 4h, an averaged effective magnetic anisotropy constant of $K_u = 265$ J m^{-3} ($|\chi| = 3300$ at $\sigma = 0$) was used.

Electrical and Magnetic sensitivity: From the FEM model, $f_r(\mu_0 H_{dc})$ and $Y(f_{ex})$ were extracted to estimate the magnitude $|Y|$ and phase angle $\arg\{Y\}$ of the admittance as functions of the alternating magnetic flux density $\mu_0 H_{ac}(t)$. In small-signal approximation at the magnetic bias field $\mu_0 H_{dc}$ and the excitation frequency f_{ex} it is

$$|Y(\mu_0 H_{ac}(t))| \approx |Y(\mu_0 H_{ac}, \mu_0 H_{dc})| + \left.\frac{\mathrm{d}|Y(f_{ex})|}{\mu_0 \mathrm{d}H}\right|_{H=H_{dc}} \mu_0 H_{ac}(t) := Y_0 + S_{am}\mu_0 H_{ac}(t) \quad (1)$$

$$\arg\{Y(\mu_0 H_{ac}(t))\} \approx \arg\{Y(\mu_0 H_{ac}, \mu_0 H_{dc})\} + \left.\frac{\mathrm{d}\arg\{Y(f_{ex})\}}{\mu_0 \mathrm{d}H}\right|_{H=H_{dc}} \mu_0 H_{ac}(t) := \phi_0 + S_{pm}\mu_0 H_{ac}(t) \quad (2)$$

with the amplitude sensitivity S_{am} and the phase sensitivity S_{pm}, which can be expressed as

$$S_{am} := \left.\frac{\mathrm{d}|Y(f_{ex})|}{\mu_0 \mathrm{d}H}\right|_{H=H_{dc}} = \left.\frac{\mathrm{d}|f_r|}{\mu_0 \mathrm{d}H}\right|_{H=H_{dc}} \left.\frac{\mathrm{d}|Y(f_{ex})|}{\mathrm{d}f_{ex}}\right|_{f_{ex}=f_r} := S_{mag}\, S_{el,am} \quad (3)$$

$$S_{pm} := \left.\frac{\mathrm{d}\arg\{Y(f_{ex})\}}{\mu_0 \mathrm{d}H}\right|_{H=H_{dc}} = \left.\frac{\mathrm{d}|f_r|}{\mu_0 \mathrm{d}H}\right|_{H=H_{dc}} \left.\frac{\mathrm{d}\arg\{Y(f_{ex})\}}{\mathrm{d}f_{ex}}\right|_{f_{ex}=f_r} := S_{mag}\, S_{el,pm} \quad (4)$$

with the magnetic sensitivity S_{mag}, the electrical amplitude sensitivity $S_{el,am}$ and electrical phase sensitivity $S_{el,pm}$.[85]

Electrical Signal Model: The small alternating to-be-measured magnetic field $\mu_0 H_{ac}(t)$ detunes the resonance frequency and shifts the admittance characteristic, which results in a modulation of the sensor's admittance Y. $f_r(\mu_0 H_{dc})$ and $Y(f_{ex})$ were extracted from the FEM model to estimate the amplitude sensitivity S_{am} and the phase sensitivity S_{pm}. The

modulated output voltage $u^*_{out}(t)$ can then be calculated with the IQ modulation scheme[84]

$$u^*_{out}(t) \approx -Z_c(f_{ex}) \cdot |u_{ex}| \cdot [Y_0 + S_{am}\mu_0 H_{ac}(t)] \cdot \cos\left(2\pi f_{ex} t + \phi_0 + S_{pm}\mu_0 H_{ac}(t)\right) \quad (5)$$

Here, $Z_c(f_{ex})$ is the impedance of the charge amplifier. The cantilever is a mechanical resonator with a finite quality factor Q and acts like a low-pass filter, which can be modeled with a first-order Bessel filter for the case $f_{ex} = f_r$.[84] Then the final output voltage amplitude can be expressed as

$$U_{out}(u_{ex}, f_{ac}) = g(f_{ac}, Q)\, U^*_{out}(u_{ex}) \quad (6)$$

with the frequency component $U^*_{out}(u_{ex})$ of the amplitude-demodulated voltage $u^*_{out}(t)$, and the magnitude response function $g(f_{ac},Q)$ of the first-order Bessel filter. Then the voltage sensitivity S_V can then be written as

$$S_V(u_{ex}, f_{ac}) = \frac{g(f_{ac}, Q)\, U^*_{out}(u_{ex})}{|\mu_0 H_{ac}(f_{ac})|} \quad (7)$$

Output Voltage Noise Model: An equivalent electrical circuit model of the ΔE-effect sensor was used for calculating the voltage output noise.[84] All the required parameters were extracted by fitting the modified Butterworth Van Dyke (mBVD)[85] model to the simulated impedance curve (Figure 2e). This equivalent circuit model includes voltage noise sources to consider thermomechanical noise, Johnson–Nyquist noise of the piezoelectric layer, quantization noise of the DA/AD converter, and noise from the charge amplifier. Except for the quantization noise, all these noise sources are independent of the excitation voltage. From the model, the total output-referred amplitude spectral densities N_e of the non-magnetic noise sources were obtained. The thermal-magnetic noise was considered with an amplitude spectral density $N_{m,th}$ and a carrier-mediated magnetic noise source with an amplitude spectral density $N_{m,c}$ was introduced. The total output noise density N_V then results from

$$N_V = \sqrt{N_e^2 + N_{m,th}^2 + N_{m,c}^2} \quad (8)$$

The magnetic noise sources were not embedded in an equivalent circuit model and were treated differently.

Thermal-Magnetic Noise: The amplitude spectral density (ASD) of the thermally excited fluctuations of magnetization M and the equivalent fluctuating magnetic flux density $\mu_0 h$ is described using the fluctuation-dissipation theorem:[60,97]

$$\mathrm{ASD}(\mu_0 h) = \sqrt{\frac{4k_B T \mu_0}{V\omega} \frac{\chi''(\omega)}{\chi'^2(\omega) + \chi''^2(\omega)}} \quad (9)$$

Here, k_B is Boltzmann constant, T is temperature, V is the volume of the sample, $\omega = 2\pi f$ is the angular frequency, $\chi = \chi' + i\chi''$ is the differential magnetic susceptibility. A detailed derivation of the Equation 9 is provided in the Supporting Information.

Derivation of Equation 9 is based on a macrospin approach assuming homogeneous magnetic properties within the volume V. Here, this equation was modified and an expression for spatially averaged thermal-magnetic noise was obtained to consider spatial inhomogeneities of the magnetic properties of the sample. The total volume V_{tot} of the magnetic layer was discretized into N elements of volumes V_i with $\sum V_i = V_{tot}$. Then, the fluctuation of the magnetic moment $\mathcal{M}$ of each element was calculated using $\mathrm{ASD}(\mathcal{M}) = V\,\mathrm{ASD}(M)$. The power spectral densities ($\mathrm{PSD} = \mathrm{ASD}^2$) were then summed up and normalized to V_{tot}. From the resulting spatially averaged ASD of the magnetization fluctuation, the corresponding ASD of the equivalent fluctuating magnetic flux density was obtained

$$\mathrm{ASD}(\mu_0 h) = \sqrt{\sum_{i=1}^{N} \frac{4k_B T \mu_0 V_i}{V_{tot}^2 \omega} \frac{\chi_i''(\omega)}{|\chi_i(\omega)|^2}} \quad (10)$$

with the differential magnetic susceptibility χ_i of the i-th element and its imaginary component χ_i''. The fluctuating thermal magnetic field in Equation 10 acts the same as the external magnetic field $\mu_0 H_{ac}$ in Equation 5 and directly modulats the carrier. Therefore, the $\mathrm{ASD}(\mu_0 h)$ is related to the output voltage via the voltage sensitivity S_V, and the amplitude spectral density $N_{m,th}$ of thermal-magnetic noise can be expressed as

$$N_{m,th} = S_V(|u_{ex}|, f)\ \mathrm{ASD}(\mu_0 h) \quad (11)$$

Carrier-Mediated Magnetic Noise: Mechanical excitation of the cantilever leads to additional carrier-mediated noise in the magnetic layer connected with the induced motion of the domain walls. In this model, it was assumed that the ASD of the carrier-mediated noise is proportional to $1/\sqrt{f}$ and depends on the spatial distribution of defects, temperature, number, and energy of the magnetic domain walls, and the stress gradient caused by the excitation. The stress gradient and the sensitivity S_V (Equation 5) scales linearly with $|u_{ex}|$ within the approximations of the signal model, which results in the following description of the amplitude spectral density of the carrier-mediated noise $N_{m,c}$:

$$N_{m,c} = A(n_{dw}, E_{dw}, P_{def}, T)\ S_V(|u_{ex}|, f)\ /\sqrt{f} \quad (12)$$

where $A(n_{dw},E_{dw},P_{def},T)$ is an effective parameter that depends on the number of active domain walls n_{dw}, their energy E_{dw}, distribution of defects P_{def} and temperature T.

Electrical Measurement Setup: All signal and noise measurements were performed with a high-resolution A/D and D/A converter (Fireface UFX+, RME, Chemnitz, Germany) at a sampling frequency of 192 kHz, using a low-noise JFET-based charge amplifier with a capacitance of 33 pF.[98] Knowing the amplifier's capacitance allowed to calculate the sensor's output current and admittance. The magnetic bias field $\mu_0 H_{dc}$ was created using a solenoid and a commercial precision current source (6221, Keithley Instruments, Solon, USA). The small alternating test magnetic field $\mu_0 H_{ac}$ was applied parallel to the bias field with a second solenoid and a second current source. The measurements were performed in a magnetically, electrically, and acoustically shielded environment.[99]

Signal and Noise Measurement Procedure: The signal and noise measurements shown in Figure 3 and Figure 4 were performed in the presence of various magnetic bias fields applied along the long axis of the cantilever. Before the measurements, a positive static magnetic field of $\mu_0 H = 6$ mT was applied along the long axis of the cantilever and then slowly decreased to the first negative magnetic bias field value $\mu_0 H_{dc}$. After finishing the signal and noise measurement procedure at one fixed magnetic bias field, the bias field was reduced to the next lower field value to repeat the procedure. At each magnetic bias field, signal and noise measurements were performed at various excitation voltage amplitudes (starting with the smallest one). After setting the excitation voltage amplitude and before the signal and noise measurements, the sensor admittance characteristic $Y(f_{ex})$ was measured to extract the resonance frequency f_r from an mBvD fit.[40,85] Then signal and noise were measured five times at $f_{ex} = f_r$ before increasing the excitation voltage amplitude.

For each signal measurement, a small sinusoidal test magnetic field $\mu_0 H_{ac}$ with $|\mu_0 H_{ac}| = 500$ nT and a frequency of $f_{ac} = 5$ Hz was applied parallel to the bias field, and the sensor's output voltage u_{out} was recorded for 20 s. For the subsequent noise measurement, the alternating test field was turned off, and u_{out} was recorded for 240 s. The amplitude spectrum U_{out} was calculated from u_{out} of the signal measurement demodulated to the baseband. The sensitivity S_V of the sensor was calculated as

$$S_V(f_{ac}) = U_{out}(f_{ac}) / |\mu_0 H_{ac}| \quad (13)$$

The amplitude spectrum density N_V of the output signal was obtained from the noise measurement, and the limit of detection (LOD) was then calculated with

$$LOD = N_V(f_{ac}) / S_V(f_{ac}) \quad (14)$$

Quasi-Static and Operando Time-Resoved Magnetooptical Imaging: Magnetic domain images in Figure 2 and Figure S2 (Supporting Information) were obtained with a home-built high-resolution bright-field magnetooptical Kerr effect (MOKE) microscope.[77] Biasing field along the long cantilever axis was created with calibrated electromagnets and a current source. For the quasi-static MOKE micrographs shown in Figure 2, a background image was recorded at the magnetically saturated state of the sample and then subtracted from the images recorded at the biasing field of interest. Images shown in Figure 2a were recorded after demagnetizing the sample in a decaying sinusoidal magnetic field. The differential susceptibility shown in Figure 2b was calculated from locally recorded MOKE magnetization curves like the one shown in Figure 2c.

For the dynamic MOKE microscopy measurements in Figure S2 (Supporting Information), a stroboscopic imaging scheme was used. A pulsed-diode laser unit (Cavilux Smart UHS, Cavitar LTD, Finland) with a pulse width of 10 ns was used as a light source. Because the pulse width was much smaller than the period of the cantilever's oscillation (ca. 125 µs), the magnetic state of the sample could be probed at each oscillation phase by changing the phase φ between the light and the excitation signal. The magnetic state was recorded at the phases φ_m and $\varphi_m + \pi$ that corresponded to the maximum and minimum induced stress in the magnetic layer. The difference between these two states showed the maximal magnetic response during the oscillation. Each image was recorded by averaging over ca. 50 000 cycles to achieve sufficient image quality in terms of signal-to-noise ratio.

Prior to the measurements, a positive saturating magnetic field $\mu_0 H_{dc} = 6$ mT was applied along the long axis of the cantilever and then slowly reduced to the bias field $\mu_0 H_{dc}$, which was kept fixed during the following measurements. Then, the cantilever was electrically excited by applying a voltage to the top electrodes using a waveform generator (DG4000, Rigol, USA). The bottom electrode was connected to the input of the charge amplifier,[98] which was, in turn, connected to the input of an A/D converter (Fireface UC+, RME, Chemnitz, Germany). The dynamic MOKE measurements were performed at various excitation voltage amplitudes (starting with $|u_{ex}| = 150$ mV). Similar to the signal and noise measurement procedure, the resonance frequency f_r was measured before each MOKE measurement. After finishing the measurement at one fixed magnetic bias field, the bias field was reduced to the next lower field value to repeat the procedure.

Supporting Information

Supporting Information is available from the Wiley Online Library or from the author.

Acknowledgements

The authors thank Christine Kirchhof and Dirk Meyners for making the ME sensor. Funding: The research was supported by the German Research Foundation (DFG) through the Collaborative Research Centre CRC 1261 "Magnetoelectric Sensors – From Composite Materials to Biomagnetic Diagnostics" and by the Carl Zeiss foundation via the project "Memristive Materials for Neuromorphic Electronics" (MemWerk).

Open access funding enabled and organized by Projekt DEAL.

Conflict of Interest

The authors declare no conflict of interest.

Author Contributions

E.S., B.S., and J.M. created the concept of the work. E.S. performed and designed the experiments. E.S. and B.S. developed the model and performed the simulations. E.S., B.S., and J.M. analyzed the results. E.S. and B.S. wrote the first version of the manuscript. All authors reviewed and revised the manuscript.

Data Availability Statement

The data that support the findings of this study are available from the corresponding author upon reasonable request.

Keywords

ΔE-effect, magnetic domains, magnetic films, magnetic sensors, magnetostriction, modeling, noise

Received: August 18, 2023
Revised: October 20, 2023
Published online: November 20, 2023

[1] R. M. Bozorth, *Bell System Techn. J.* **1940**, *19*, 1.
[2] R. C. O'Handley, *Modern Magnetic Materials: Principles and Applications*, John Wiley, New York **2000**.
[3] G. Herzer, *Acta Mater.* **2013**, *61*, 718.
[4] A. Renuka Balakrishna, R. D. James, *Appl. Phys. Lett.* **2021**, 118.
[5] A. Renuka Balakrishna, R. D. James, *NPJ Comput Mater* **2022**, *8*, 4.
[6] P. Ripka, K. Závěta, in *Handbook of Magnetic Materials*, (Ed.: K. Buschow), Elsevier, **2009**, Vol. *18*, p. 347.
[7] R. Hunt, *IEEE Trans Magn* **1971**, *7*, 150.
[8] C. H. Lin, P. C. Kuo, J. S. Huang, *IEEE Trans Magn* **1995**, *31*, 2916.
[9] T. McGuire, R. Potter, *IEEE Trans Magn* **1975**, *11*, 1018.
[10] D. E. Heim, R. E. Fontana, C. Tsang, V. S. Speriosu, B. A. Gurney, M. L. Williams, *IEEE Trans Magn* **1994**, *30*, 316.
[11] B. Dieny, V. S. Speriosu, S. S. Parkin, B. A. Gurney, D. M. Wilhoit, *Phys Rev B Condens Matter* **1991**, *43*, 1297.
[12] J. C. S. Kools, *IEEE Trans Magn* **1996**, *32*, 3165.
[13] G. Binasch, P. Grünberg, F. Saurenbach, W. Zinn, *Physica B Condens Matter* **1989**, *39*, 4828.
[14] M. N. Baibich, J. M. Broto, A. Fert, F. N. Van Dau, F. Petroff, P. Etienne, G. Creuzet, A. Friederich, J. Chazelas, *Phys. Rev. Lett.* **1988**, *61*, 2472.
[15] J.-G. Zhu, C. Park, *Mater. Today* **2006**, *9*, 36.
[16] S. S. P. Parkin, C. Kaiser, A. Panchula, P. M. Rice, B. Hughes, M. Samant, S.-H. Yang, *Nature Mater* **2004**, *3*, 862.
[17] S. Kämmerer, A. Thomas, A. Hütten, G. Reiss, *Appl. Phys. Lett.* **2004**, *85*, 79.
[18] D. Karnaushenko, D. D. Karnaushenko, D. Makarov, S. Baunack, R. Schäfer, O. G. Schmidt, *Adv. Mater.* **2015**, *27*, 6582.
[19] K. Mohri, T. Uchiyama, L. V. Panina, M. Yamamoto, K. Bushida, *Journal of Sensors* **2015**, *2015*, 718069.
[20] K. Mohri, K. Kawashima, T. Kohzawa, H. Yoshida, *IEEE Trans Magn* **1993**, *29*, 1245.
[21] C. Dong, X. Liang, J. Gao, H. Chen, Y. He, Y. Wei, M. Zaeimbashi, A. Matyushov, C. Sun, N. X. Sun, *Adv. Electron. Mater.* **2022**, *8*, 2200013.
[22] E. Lage, C. Kirchhof, V. Hrkac, L. Kienle, R. Jahns, R. Knöchel, E. Quandt, D. Meyners, *Nature Mater* **2012**, *11*, 523.
[23] Y. Wang, J. Li, D. Viehland, *Mater. Today* **2014**, *17*, 269.
[24] M. Fiebig, *J. Phys. D: Appl. Phys.* **2005**, *38*, R123.
[25] A. Kittmann, P. Durdaut, S. Zabel, J. Reermann, J. Schmalz, B. Spetzler, D. Meyners, N. X. Sun, J. McCord, M. Gerken, G. Schmidt, M. Höft, R. Knöchel, F. Faupel, E. Quandt, *Sci. Rep.* **2018**, *8*, 278.
[26] T. Nan, H. Lin, Y. Gao, A. Matyushov, G. Yu, H. Chen, N. Sun, S. Wei, Z. Wang, M. Li, X. Wang, A. Belkessam, R. Guo, B. Chen, J. Zhou, Z. Qian, Y. Hui, M. Rinaldi, M. E. Mcconney, B. M. Howe, Z. Hu, J. G. Jones, G. J. Brown, N. X. Sun, *Nat. Commun.* **2017**, *8*, 296.
[27] Z. Marinho, S. Cardoso, R. Chaves, R. Ferreira, L. V. Melo, P. P. Freitas, *J. Appl. Phys.* **2011**, *109*, 07E521.
[28] A. S. Edelstein, G. A. Fischer, M. Pedersen, E. R. Nowak, S. F. Cheng, C. A. Nordman, *J. Appl. Phys.* **2006**, *99*.

[29] M. A. Caro, S. Zhang, T. Riekkinen, M. Ylilammi, M. A. Moram, O. Lopez-Acevedo, J. Molarius, T. Laurila, *J. Phys.: Condens. Matter* **2015**, *27*, 245901.
[30] J. Zhang, P. Li, Y. Wen, W. He, A. Yang, C. Lu, *Smart Mater. Struct.* **2014**, *23*, 95028.
[31] Q. Zhang, in *Advanced Materials for Electromagnetic Shielding*, (Eds.: M. Jaroszewski, S. Thomas, A. V. Rane), p. 109.
[32] J. F. Hoburg, *IEEE Trans. Electromagn. Compat.* **1995**, *37*, 574.
[33] P. M. Drljaca, F. Vincent, P.-A. Besse, R. S. Popovic, *Sens. Actuators, A* **2002**, *97–98*, 10.
[34] C. Zheng, K. Zhu, S. Cardoso de Freitas, J.-Y. Chang, J. E. Davies, P. Eames, P. P. Freitas, O. Kazakova, C. Kim, C.-W. Leung, S.-H. Liou, A. Ognev, S. N. Piramanayagam, P. Ripka, A. Samardak, K.-H. Shin, S.-Y. Tong, M.-J. Tung, S. X. Wang, S. Xue, X. Yin, P. W. T. Pong, *IEEE Trans Magn* **2019**, *55*, 0800130.
[35] E. Elzenheimer, C. Bald, E. Engelhardt, J. Hoffmann, P. Hayes, J. Arbustini, A. Bahr, E. Quandt, M. Höft, G. Schmidt, *Sensors* **2022**, *22*, 1018.
[36] Y. Wang, D. Gray, D. Berry, J. Gao, M. Li, J. Li, D. Viehland, *Adv. Mater.* **2011**, *23*, 4111.
[37] A. van der Ziel, in *Advances in Electronics and Electron Physics*, Vol. *49* (Eds.: L. Marton, C. Marton), Academic Press, xx xx **1979**, p. 225.
[38] Y. Hou, D. F. Wang, T. Itoh, *Measurement* **2023**, *207*, 112396.
[39] P. Hayes, M. Jovicevic Klug, S. Toxværd, P. Durdaut, V. Schell, A. Teplyuk, D. Burdin, A. Winkler, R. Weser, Y. Fetisov, M. Höft, R. Knöchel, J. McCord, E. Quandt, *Sci. Rep.* **2019**, *9*, 16355.
[40] S. Zabel, C. Kirchhof, E. Yarar, D. Meyners, E. Quandt, F. Faupel, *Appl. Phys. Lett.* **2015**, *107*, 152402.
[41] H. Weitensfelder, H. Brueckl, A. Satz, K. Pruegl, J. Zimmer, S. Luber, W. Raberg, C. Abert, F. Bruckner, A. Bachleitner-Hofmann, R. Windl, D. Suess, *Phys. Rev. Appl.* **2018**, *10*, 54056.
[42] P. Durdaut, E. Rubiola, J.-M. Friedt, C. Muller, B. Spetzler, C. Kirchhof, D. Meyners, E. Quandt, F. Faupel, J. McCord, R. Knochel, M. Hoft, *J. Microelectromech. Syst.* **2020**, *29*, 1347.
[43] W. F. Egelhoff, P. W. T. Pong, J. Unguris, R. D. Mcmichael, E. R. Nowak, A. S. Edelstein, J. E. Burnette, G. A. Fischer, *Sens. Actuators, A* **2009**, *155*, 217.
[44] R. H. Koch, J. G. Deak, G. Grinstein, *Appl. Phys. Lett.* **1999**, *75*, 3862.
[45] N. Smith, P. Arnett, *IEEE Trans Magn* **2002**, *38*, 32.
[46] B. Dufay, E. Portalier, S. Saez, C. Dolabdjian, D. Seddaoui, A. Yelon, D. Menard, *IEEE Trans Magn* **2017**, *53*, 4000106.
[47] H. N. Bertram, Zhen Jin, V. L. Safonov, *IEEE Trans Magn* **2002**, *38*, 38.
[48] P. Dhagat, A. Jander, C. A. Nordman, *J. Appl. Phys.* **2005**, *97*, 10C911.
[49] M. Xiao, K. B. Klaassen, J. C. L. Van Peppen, M. H. Kryder, *J. Appl. Phys.* **1999**, *85*, 5855.
[50] J. L. Liou, P. J. Wei, W. L. Liang, C. F. Ai, J. F. Lin, *J. Appl. Phys.* **2008**, *103*, 07E920.
[51] L. Chen, J. Fernandez-de-Castro, J. Giusti, H. Fang, M. Hurben, *J. Appl. Phys.* **2000**, *36*, 3195.
[52] J. Zhang, N. Zhu, Y. Huai, A. Prabhakar, P. Rana, D. Seagle, M. Lederman, *IEEE Trans Magn* **2001**, *37*, 1678.
[53] P. Durdaut, C. Müller, A. Kittmann, V. Schell, A. Bahr, E. Quandt, R. Knöchel, M. Höft, J. McCord, *Sensors* **2021**, *21*, 5631.
[54] A. K. Raychaudhuri, *Curr Opin Solid State Mater Sci* **2002**, *6*, 67.
[55] D. V. Berkov, in *Handbook of Magnetism and Advanced Magnetic Materials*, (Eds.: H. Kronmüller, S. S. P. Parkin), John Wiley & Sons, Hoboken, NJ **2007**, Vol. *2*, p. 1.
[56] R. F. L. Evans, U. Atxitia, R. W. Chantrell, *Phys. Rev. B* **2015**, *91*, 144425.
[57] J. Leliaert, J. Mulkers, J. De Clercq, A. Coene, M. Dvornik, B. Van Waeyenberge, *AIP Adv.* **2017**, *7*, 125010.
[58] R. F. L. Evans, W. J. Fan, P. Chureemart, T. A. Ostler, M. O. A. Ellis, R. W. Chantrell, *J. Phys.: Condens. Matter* **2014**, *26*, 103202.
[59] L. G. C. Melo, D. Ménard, A. Yelon, L. Ding, S. Saez, C. Dolabdjian, *J. Appl. Phys.* **2008**, *103*, 33903.
[60] L. Reggiani, E. Alfinito, *Fluct. Noise Lett* **2019**, *18*, 1930001.
[61] R. Zwanzig, *Annu. Rev. Phys. Chem.* **1965**, *16*, 67.
[62] Y. Cheng, B. Peng, Z. Hu, Z. Zhou, M. Liu, *Phys. Lett. A* **2018**, *382*, 3018.
[63] A. B. Flatau, B. J. Stadler, J. Park, K. S. M. Reddy, P. R. Downey, C. Mudivarthi, M. van Order, in *Magnetic Nano- and Microwires: Design, Synthesis, Properties and Applications* (Ed.: M. Vázquez), Woodhead Publishing, London, UK **2020**, p. 737.
[64] V. Apicella, C. S. Clemente, D. Davino, D. Leone, C. Visone, *Actuators* **2019**, *8*, 45.
[65] H. Wu, T. Jiang, Z. Liu, S. Fu, J. Cheng, H. You, J. Jiao, M. Bichurin, O. Sokolov, S. Ivanov, Y. Wang, *Adv. Electron. Mater.* **2023**.
[66] J. Xu, C. Leung, X. Zhuang, J. Li, S. Bhardwaj, J. Volakis, D. Viehland, *Sensors* **2019**, *19*, 853.
[67] A. Chen, R.-C. Peng, B. Fang, T. Yang, Y. Wen, D. Zheng, C. Zhang, C. Liu, Z. Li, P. Li, Y. Li, Y. Zhao, C.-W. Nan, Z. Qiu, L.-Q. Chen, X.-X. Zhang, *Adv. Funct. Mater.* **2023**, *33*, 2213402.
[68] T. Nan, J.-M. Hu, M. Dai, S. Emori, X. Wang, Z. Hu, A. Matyushov, L.-Q. Chen, N. Sun, *Adv. Funct. Mater.* **2019**, *29*, 1806371.
[69] H.-C. Chang, S.-C. Liao, H.-S. Hsieh, J.-H. Wen, C.-H. Lai, W. Fang, *Sens. Actuators, A* **2016**, *238*, 25.
[70] D. Meyners, T. Von Hofe, M. Vieth, M. Rührig, S. Schmitt, E. Quandt, *J. Appl. Phys.* **2009**, *105*, 07C914.
[71] J. J. Park, K. S. M. Reddy, B. Stadler, A. Flatau, *IEEE Sens. J.* **2017**, *17*, 2015.
[72] P. Hayes, V. Schell, S. Salzer, D. Burdin, E. Yarar, A. Piorra, R. Knöchel, Y. K. Fetisov, E. Quandt, *J. Phys. D: Appl. Phys.* **2018**, *51*, 354002.
[73] N. Lukat, R.-M. Friedrich, B. Spetzler, C. Kirchhof, C. Arndt, L. Thormählen, F. Faupel, C. Selhuber-Unkel, *Sens. Actuators, A* **2020**, *309*, 112023.
[74] A. D. Matyushov, B. Spetzler, M. Zaeimbashi, J. Zhou, Z. Qian, E. V. Golubeva, C. Tu, Y. Guo, B. F. Chen, D. Wang, A. Will-Cole, H. Chen, M. Rinaldi, J. McCord, F. Faupel, N. X. Sun, *Adv. Mater. Technol.* **2021**, *6*, 2100294.
[75] S. Zabel, J. Reermann, S. Fichtner, C. Kirchhof, E. Quandt, B. Wagner, G. Schmidt, F. Faupel, *Appl. Phys. Lett.* **2016**, *108*, 222401.
[76] Spetzler, Golubeva, Müller, McCord, Faupel, *Sensors* **2019**, *19*, 4769.
[77] J. McCord, *J. Phys. D: Appl. Phys.* **2015**, *48*, 333001.
[78] A. Aharoni, *phys. stat. sol.(b)* **2002**, *229*, 1413.
[79] N. O. Urs, I. Teliban, A. Piorra, R. Knöchel, E. Quandt, J. McCord, *Appl. Phys. Lett.* **2014**, *105*, 202406.
[80] A. Hubert, R. Schäfer, *Magnetic Domains: The Analysis of Magnetic Microstructures*, Springer Berlin, Berlin **1998**.
[81] S. Middelhoek, *IBM J. Res. Dev.* **1962**, *6*, 394.
[82] J. Steiner, R. Schäfer, H. Wieczoreck, J. McCord, F. Otto, *Phys. Rev. B* **2012**, *85*, 104407.
[83] C. Tsang, S. K. Decker, *J. Appl. Phys.* **1981**, *52*, 2465.
[84] B. Spetzler, P. Wiegand, P. Durdaut, M. Höft, A. Bahr, R. Rieger, F. Faupel, *Sensors* **2021**, *21*, 7594.
[85] B. Spetzler, J. Su, R.-M. Friedrich, F. Niekiel, S. Fichtner, F. Lofink, F. Faupel, *APL Mater.* **2021**, *9*, 31108.
[86] Z. Chu, C. Dong, C. Tu, Y. He, X. Liang, J. Wang, Y. Wei, H. Chen, X. Gao, C. Lu, Z. Zhu, Y. Lin, S. Dong, J. McCord, N.-X. Sun, *Phys. Rev. Appl.* **2019**, *12*, 44001.
[87] B. Spetzler, Ph.D. Thesis **2022**.
[88] J. Mccord, J. Westwood, *IEEE Trans Magn* **2001**, *37*, 1755.
[89] H. Clow, *Nature* **1962**, *194*, 1035.
[90] M. Labrune, J. Miltat, *J. Magn. Magn. Mater.* **1995**, *151*, 231.
[91] D. Punz, J. Lee, M. Fuger, J. Fidler, T. Schrefl, D. Suess, *J. Appl. Phys.* **2010**, *107*, 113926.
[92] A. Ludwig, E. Quandt, *IEEE Trans Magn* **2002**, *38*, 2829.
[93] S. Avdiaj, J. Setina, N. Syla, *Materials and technology* **2009**, *43*, 283.
[94] (Ed.: J. Yang), *An Introduction to the Theory of Piezoelectricity*, Springer, Cham **2018**.

[95] IEEE, *IEEE Trans. Sonics Ultrason.* **1973**, *20*, 67.
[96] B. Spetzler, E. V. Golubeva, R.-M. Friedrich, S. Zabel, C. Kirchhof, D. Meyners, J. McCord, F. Faupel, *Sensors* **2021**, *21*, 2022.
[97] R. Kubo, *Rep Prog Phys* **1966**, *29*, 255.
[98] P. Durdaut, V. Penner, C. Kirchhof, E. Quandt, R. Knochel, M. Hoft, *IEEE Sens. J.* **2017**, *17*, 7364.
[99] S. Marauska, R. Jahns, H. Greve, E. Quandt, R. Knöchel, B. Wagner, *J. Micromech. Microeng.* **2012**, *22*, 065024.